ACS OMEGA

http://pubs.acs.org/journal/acsodf

Article

Nonisocyanate Poly(Hydroxyl Urethane)-Based Green Polymer Hybrid Coating Systems: Tailoring of Biomacromolecular Compound Architecture Using APTMS-ZnO/TEMPO-Oxidized Cellulose Nanoparticles

Mhd. Abd. Cader Mhd. Haniffa, Hazlee Azil Illias,* Ching Yern Chee,* Shaliza Ibrahim, Viorel Sandu, and Cheng Hock Chuah

Cite This: *ACS Omega* 2020, 5, 10315−10326

Read Online

ACCESS | Metrics & More | Article Recommendations | Supporting Information

ABSTRACT: Hybrid bionanocomposite coating systems (HBCSs) are green polymer materials consisting of an interface between a coating matrix and nanoparticles. The coating matrix was prepared by using a nonisocyanate poly(hydroxyl urethane) (NIPHU) prepolymer crosslinked via 1,3-diaminopropane and epoxidized *Jatropha curcas* oil. TEMPO-oxidized cellulose nanoparticles (TARC) were prepared from microcrystalline cellulose, and (3-aminopropyl)trimethoxysilane (APTMS)-coated ZnO nanoparticles (APTMS-ZnO) and their suspensions were synthesized separately. The suspensions at different weight ratios were incorporated into the coating matrix to prepare a series of HBCSs. FT-IR, ^{1}H-NMR, ^{13}C-NMR, XRD, SEM, and TEM were used to confirm the chemical structures, morphology, and elements of the coating matrix, nanomaterials, and HBCSs. The thermomechanical properties of the HBCSs were investigated by TGA-DTG and pencil hardness analyses. The UV and IR absorption spectra of the HBCSs were obtained using UV−vis spectroscopy and FTIR spectroscopy, respectively. The HBCSs exhibited good thermal stability at about 200 °C. The degradation temperature at 5% mass loss of all samples was over around 280 °C. The HBCSs exhibited excellent UV block and IR active properties with a stoichiometric ratio of the NIPHU prepolymer and EJCO of 1:1 (wt/wt) containing 5 wt % TARC and 15 wt % APTMS-ZnO nanoparticles. It was observed that the sample with 5 wt % TARC and 15 wt % APTMS-ZnO (HBCS-2) exhibited a uniform crosslinking and reinforcement network with a T_{onset} of 282 °C. This sample has successfully achieved good coating hardness and excellent UV and IR absorption.

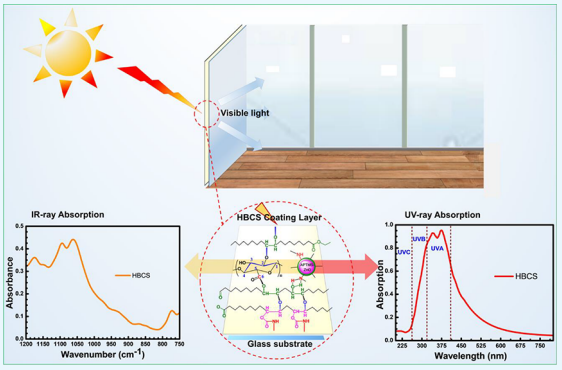

INTRODUCTION

The present perspective of the development of sustainable biobased chemistry and greener components of polymer materials has attracted both industrial and research-oriented applications.[1−3] Hybrid nanocomposite coatings are a novel class of advance materials containing both a coating matrix and nanoparticles. A potential combination of the advantages of inorganic materials including high thermal and chemical stability, high hardness, high refractive index, etc. with those of the coating matrix such as processability, flexibility, low weight, etc. can enable a wide range of applications for these nanocomposites. The applications range from conventional plastics reinforcement to abrasion-resistant coatings,[4,5] optical devices,[6,7] catalysis,[8,9] memory devices,[10] electrical insulation in microelectronics and nanodielectrics,[11,12] integral capacitors,[13] fuel cells,[14] flame-retardant materials,[15,16] etc. However, in terms of bio-based hybrid nanocomposite coating, vegetable oils and nonisocyanate poly(hydroxyl urethane) (NIPHU)-based fabrication methods have widely attracted researchers and academics during the past few decades. NIPHU is an alternative green chemistry approach that can replace toxic isocyanate-based polyurethane production. However, the hydroxyl groups positioned at the α- and β-carbon in the NIPHU moiety promote adhesiveness and steric hindrance among polyurethane macromolecules.[17] Furthermore, the NIPHU networks become weaker owing to the steric hindrance of their hydroxyl moieties. Therefore, a casting temperature above 100 °C and a longer curing time are required[18−20] to prepare NIPHU-based polymer materials. A recent study has reported a temperature of about 120 °C for the curing process to obtain NIPHU thick film materials.[21]

Received: December 20, 2019
Accepted: April 13, 2020
Published: May 1, 2020

https://dx.doi.org/10.1021/acsomega.9b04388
ACS Omega 2020, 5, 10315−10326

Hence, it is possible to form NIPHU films at temperatures below 100 °C if their hydroxyl groups were coupled with some other functional nanomaterials.

Consequently, these functional nanomaterials can form covalent and/or strong hydrogen bonds along the polymeric backbone of the coating matrix. For example, to obtain high specific strength and promising reinforcing properties, organic polymer fillers, especially cellulose nanocrystals (CNCs), have been embedded in a wide range of polymer matrices.[22] CNCs exhibit a series of advantages, including high capacity to modify their surface by employing various functional molecules.[23−28] In this regard, enhancement of the thermostructural properties of the TEMPO-oxidized/rapid cooled CNC (TEMPO/RC-CNC) has been reported recently.[29] The authors claimed that the additional rapid cooling (RC) treatment has significantly improved their material properties.[29] However, a TEMPO/RC-CNC-based reinforcement study of NIPHU was not reported until the present investigation.

On the other hand, inorganic nanoscale metal oxides such as ZnO, CeO_2, and TiO_2 are excellent UV-cutoff metal oxides, which provide photoprotection by scattering, reflecting, and absorbing UV photons.[30] Nonetheless, there are still some adverse effects such as the photocatalytic activity of these metal oxides, which degrades the polymer matrix of the nanocomposite coating. When these nanocomposites are exposed to UV irradiation, the weight accumulation in the nanocomposite may alter the mechanical properties, especially the elongation at break of the nanocomposite. However, the photocatalytic activity of these metal oxides can be minimized by introducing a barrier coating layer on the surface of the metal oxides. Thus, the nanocomposite film can be protected from the photodegradation effect. By considering all these facts, efforts have been made to study the synergistic effect of the TEMPO/RC-CNC (TARC) and APTMS-ZnO NPs on IR and UV absorption, and thermomechanical properties of the HBCS network. Furthermore, the optimum level of IR and UV absorption of the HBCS coating was determined in this study.

RESULTS AND DISCUSSION

Structural Harmonics of Epoxidation and 5-Membered Cyclic Carbonate of *J. curcas* Oil. The formation of CJCO via epoxidation is illustrated in the FTIR spectra (Figure 1). The C═O stretching vibration band of JCO was shifted from 1745 toward 1738 cm^{-1} after cyclic carbonation. The peak of −CH═CH− at 1712 cm^{-1} was replaced by the epoxy ring with peaks at 846 and 823 cm^{-1} (circled in Figure 1), and a characteristic peak of carbonate carbonyl at 1805 cm^{-1} appeared. Moreover, $-CH_2$ scissoring and −C−O stretching of the ester can be observed at 1464 and 1167 cm^{-1}, respectively.[17]

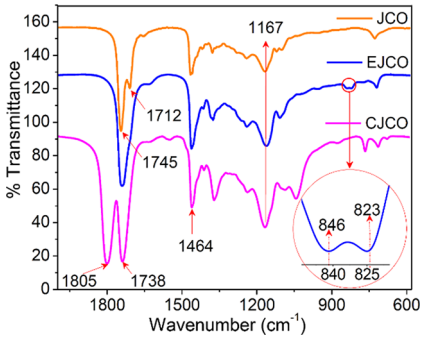

Figure 1. FTIR spectra of the conversion of JCO into the CJCO precursor via epoxidized JCO (EJCO).

Characterizations of TARC NPs. A characteristic peak of the C═O stretching vibration of dimeric carboxyl groups was observed at 1728 cm^{-1} after RC (Figure 2a). The band at 1430 cm^{-1} was assigned to the crystalline nature, whereas the peak at 895 cm^{-1} was attributed to the amorphous system.[31] In-plane and out-plane deformations such as twisting, wagging, or stretching vibration of the different groups in nanocelluloses such as C−O, C−H, −O−H, and C−O groups were observed at 1160, 1111, and 1035 cm^{-1} respectively[17,32]

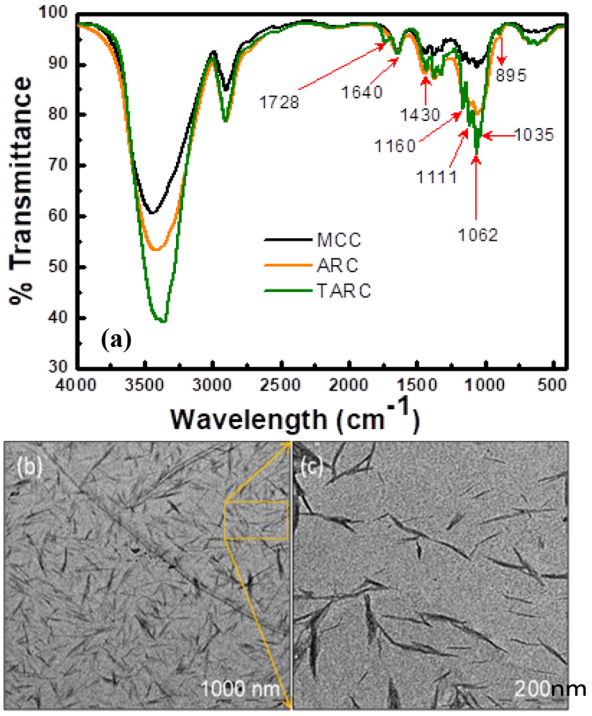

Figure 2. (a) FT-IR spectra of the MCC (microcrystalline cellulose), ARC (acid hydrolyzed and rapidly cooled cellulose nanocrystal), and TARC (TEMPO/RC-ARC); (b) TEM images of the TEMPO/RC-CNC (TARC) with different magnifications 1000 nm and (c) 200 nm.

TEM of TARC NPs was performed to investigate their morphology (Figure 2b,c) at two different magnifications. The nanocrystals were long and slender with a rod-like morphology and an average aspect ratio (length/width) of 13.22.

Characterization of APTMS-ZnO NPs. The peak at 3459 cm^{-1} was assigned to the hydroxyl (−OH) stretching vibrations[28,29] of the ZnO NPs, as shown in the upper spectrum (blue line) (Figure 3a). It was observed that after successful APTMS functionalization over ZnO NPs, the peak corresponding to the −OH group overlapped with the corresponding peak of the N−H groups further and relocated into 3239 and 3136 cm^{-1}, as illustrated in the lower spectrum (pink line) (Figure 3a).

These stretching vibration peaks confirmed that the alkyd chain was present at the end terminal in APTMS having a secondary amine after functionalization on the ZnO surface. The characteristic peaks at 2923 and 2882 cm^{-1} correspond to the symmetric and asymmetric C−H stretching of the alkyd chain present in APTMS. The corresponding peaks of the

https://dx.doi.org/10.1021/acsomega.9b04388
ACS Omega 2020, 5, 10315−10326

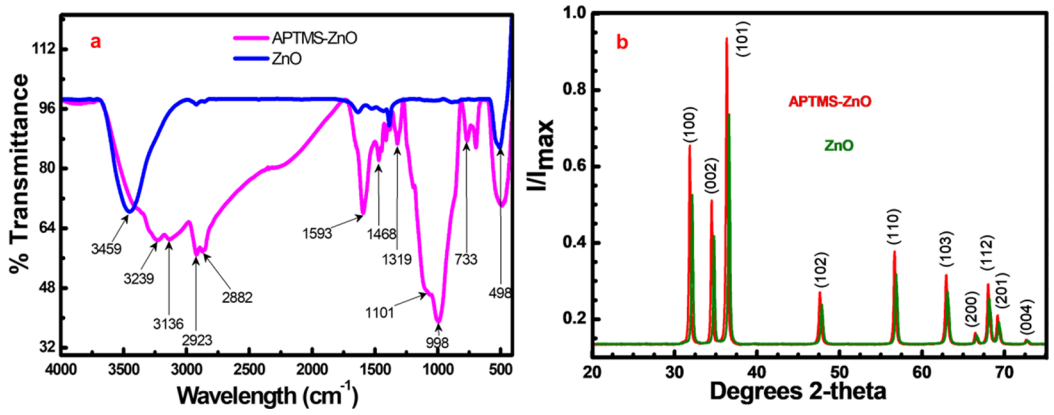

Figure 3. FT-IR spectra of (a) as-prepared ZnO (line in blue color) and APTMS-treated ZnO (line in pink color) NPs and (b) X-ray diffraction patterns of ZnO NPs (green line) and APTMS-treated (basic condition) ZnO NPs (red line).

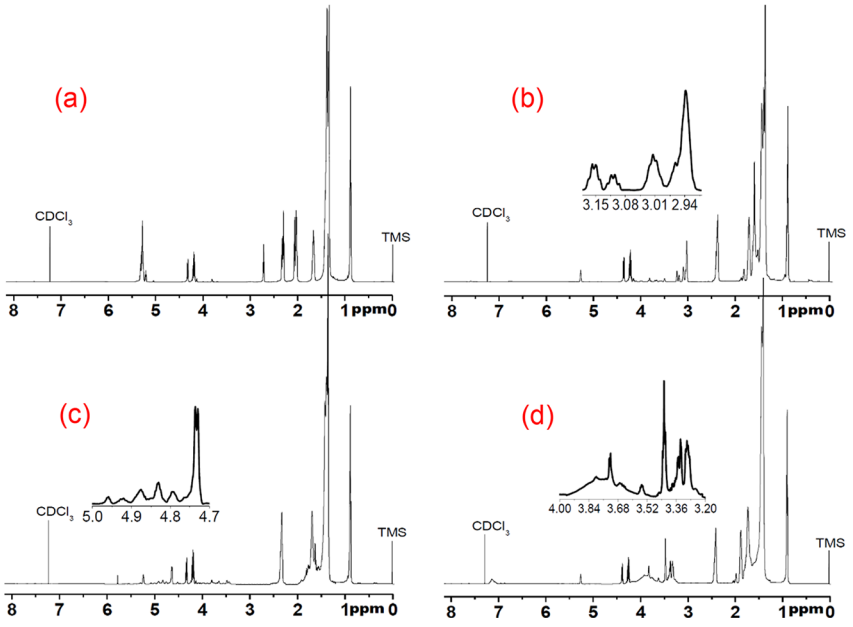

Figure 4. ^{1}H-NMR spectra of (a) *J. curcas* oil (JCO), (b) epoxidized *J. curcas* oil (EJCO), (c) 5-membered cyclic carbonated *J. curcas* oil (CJCO), (d) coating matrix of the nonisocyanate poly (hydroxyl urethane) prepolymer and EJCO (NIPUB).

bending vibration of the C−O groups and out-of-plane bending vibration of N−H were observed at 1593 and 1468 cm^{-1}, respectively. Moreover, the influential broad and sharp consecutive bands, which were seen at 1319, 1101, 998, 753, and 498 cm^{-1}, were attributed to the C−H in-plane bending and symmetrical stretching vibrations of the Si−O−Si bonds, Zn−O−Si bonds, N−H wagging, and Zn−O stretching vibrations, respectively.[33] The capping and the formation of covalent bonds between the ZnO NPs and −Si−O− layer of APTMS were confirmed by the presence of Zn-O-Si stretching vibrations.[34]

All diffraction peaks in the XRD pattern of the APTMS-ZnO NPs (Figure 3b) were assigned to the hexagonal wurtzite structure of ZnO with lattice parameters a = 3.2417, b = 3.2417, and c = 5.1876 Å according to JCPDS card 01-079-0205, and the data were in good agreement with previous studies. The data were in good agreement with previous work, and the difference between the XRD patterns of ZnO and APTMS-ZnO NPs was not observed (Figure 3b).[34,35] The average particle size of 33.00 nm was calculated using the Scherrer formula. The absence of any new peak and the identical intensity ratio I/I_{max} suggested that the preparation process of APTMS-ZnO changes neither the structure nor the shape of ZnO NPs.[34]

Spectroscopic Analysis of the HBCS. The peak at chemical shift of 7.24−7.25 ppm was attributed to the solvent observed in all spectra. The ^{1}H-NMR spectrum of *Jatropha curcas* oil showed peaks between 5.5−5.32 ppm and 5.32−5.25 ppm, which were assigned to the C=C moiety and the sn−2 glycerol proton, respectively (Figure 4a). The peak at 4.34 ppm was attributed to the sn−1 and sn−3 glycerol protons. The characteristic peaks for the bisallylic proton of C18:2 and allylic protons of C18:2 and C18:1 were observed at 2.85−2.75 ppm and 2.1−2.0 ppm, respectively.

The −CH$_2$ proton adjacent to C=O groups was visible at 2.4−2.3 ppm. The peak at 1.69−1.58 ppm was due to the proton −CH$_2$, attached at the β-position of the fatty acid chain (Figure 4a). The protons of all the internal CH$_2$ groups present in the fatty acid chain were observed at 1.41−1.24 ppm. The corresponding peak of the protons of the terminal methyl groups appeared at 0.93−0.88 ppm (Figure 4a). The ^{1}H-NMR spectrum of EJCO showed a peak region of 5.5−5.32

https://dx.doi.org/10.1021/acsomega.9b04388
ACS Omega 2020, 5, 10315−10326

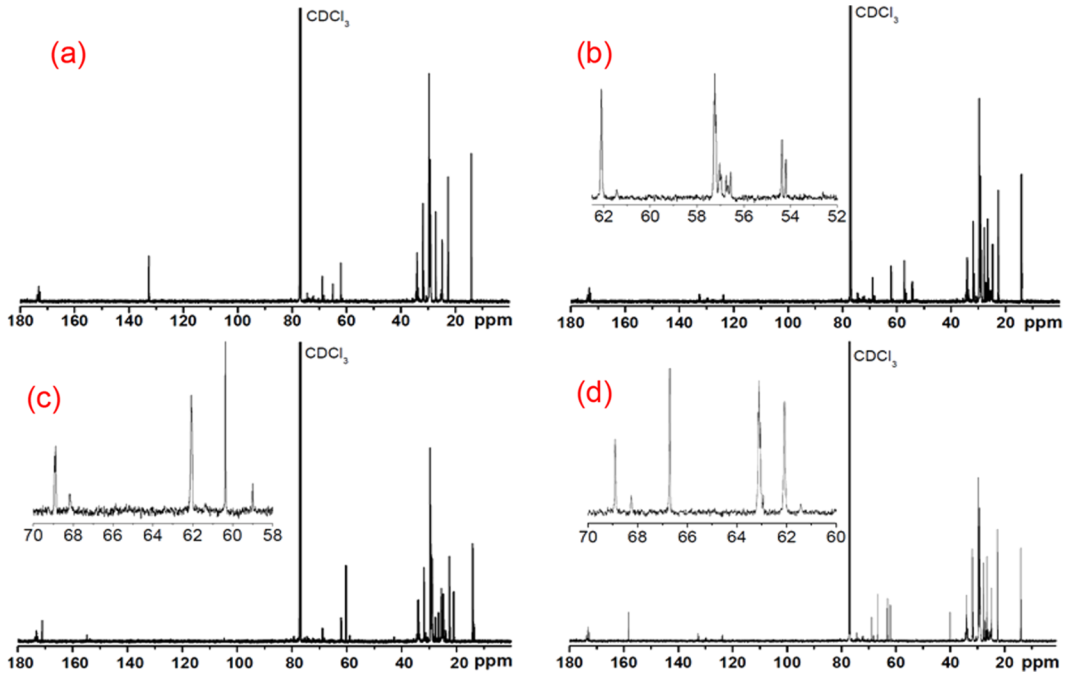

Figure 5. ^{13}C-NMR spectra of (a) JCO, (b) EJCO, (c) CJCO, and (d) NIPUB.

Scheme 1. Biomacromolecular Polymer Network of HBCS Incorporated with TARC and APTMS-ZnO Nanoparticles

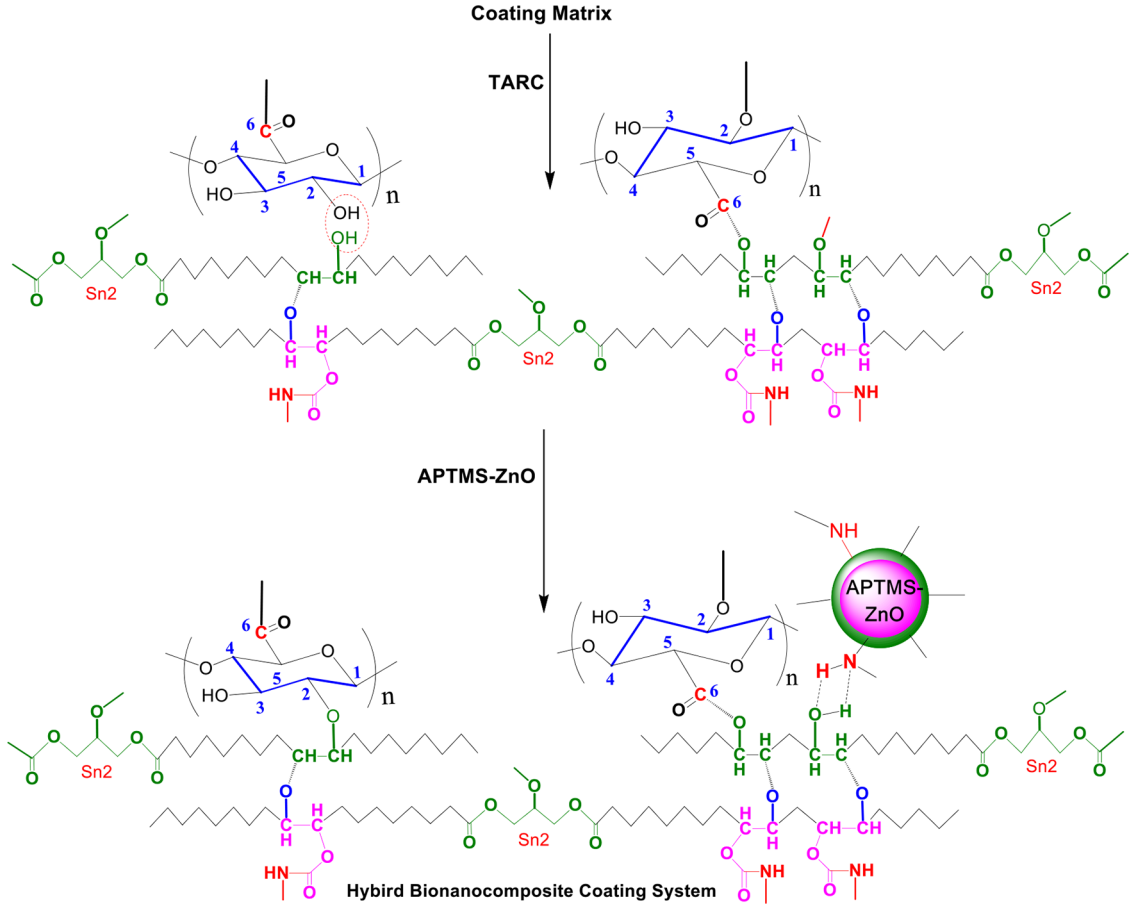

ppm, which was related to the disappearance of C═C with the formation of new peaks at 3.16−3.08, 3.08−2.96, and 2.96−2.89 ppm (Figure 4b). These peaks correspond to the protons of diepoxides of linoleic acid and epoxides of linoleic acid and their overlap to the epoxy oleic acid, respectively. However, in the ^{1}H-NMR spectrum of CJCO (Figure 4c), the peaks at 3.16−2.89 ppm, which was associated with epoxy protons, were observed to disappear with the formation of new peaks at

https://dx.doi.org/10.1021/acsomega.9b04388
ACS Omega 2020, 5, 10315−10326

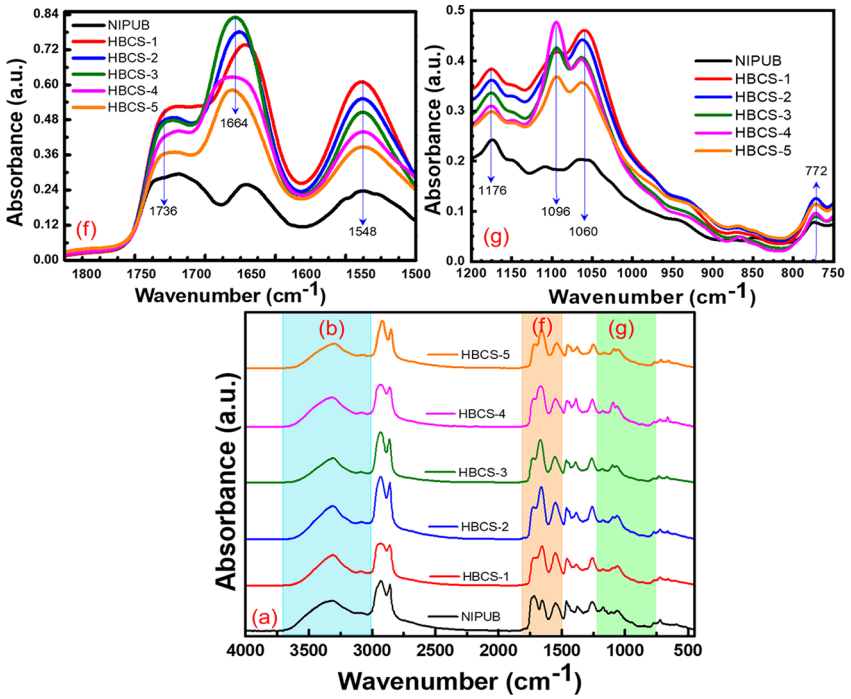

Figure 6. FTIR spectra of (a) bionanocomposite coating incorporated with TARC-4 and APTMS-ZnO nanoparticles; (b) −O−H and −N−H stretching region; (f) urethane formation region; and (g) IR-absorption region.

5.06−4.52 ppm corresponding to the protons of the CJCO groups.

New peaks appeared at 4.00−3.20 ppm in the ^{1}H-NMR spectrum of the coating matrix (Figure 4d), which was confirmed by the completion of the epoxy ring-opening reaction of EJCO with the hydroxyl groups of the NIPHU prepolymer. The spectrum did not show any peak of the epoxy and carbonate carbonyl groups. This result indicated the complete consumption of the epoxy groups by hydroxyl groups of the NIPHU prepolymer. The peak at 7.11−7.21 ppm corresponds to the −NH protons of the urethane groups.

Besides, the successful hybridization of the EJCO and NIPHU prepolymer by ring-opening and polymerization was evidenced by the ^{13}C-NMR investigation. The peak of the unsaturated carbon atoms at 132 ppm disappeared (Figure 5a) with the formation of a new peak at 57.3−56.5 ppm (Figure 5b), which was attributed to the carbon atoms of the epoxy groups. Additionally, a new peak at 60.8 ppm assigned to the carbonyl carbon of CJCO was observed, and there was no peak corresponding to the carbon atoms on epoxy groups(Figure 5c). The spectrum (Figure 5d showed new peaks at 66.8 ppm and 63.4 ppm resulting from the action of carbon atoms adjacent to the −O and −N atoms of the urethane group. The ^{13}C-NMR peak of the carbonyl carbon atoms of urethane groups was observed at 158 ppm (Figure 5d). However, both of the peaks corresponding to the carbon atoms of unsaturated, epoxy, and carbonate carbonyl groups were not present in the ^{13}C-NMR spectrum of the NIPUB (Figure 5d).

Effect of NPs on the HBCS Polymer Network. The condensation of the −OH groups of the TARC and the polymer network created an ether link, as illustrated in Scheme 1. The formation of this ester link decreased the −OH stretching vibration of the coating spectra. The drop of the corresponding FTIR signal (Figure 6b) with the increase of the TARC content, i.e., from HBCS-1 to HBCS-5, confirmed this fact. In contrast, the sample HBCS-1 exhibited a significant peak of the −NH stretching vibration at 3300 cm^{-1}, whereas no significant change was observed in the corresponding peaks of other samples. The effect of the TARC and APTMS-ZnO NPs on the polymer network of the HBCS was visible in the changes of the urethane stretching frequency (Figure 6c). The peaks at 1736 and 1736−1664 cm^{-1} were attributed to the carbonyl and urethane groups of the polymer network. The incorporation of TARC NPs increased the peak intensity.

Consequently, sample HBCS-5 exhibited a higher peak intensity compared to the pristine NIPUB, whereas this was not noticeable in the HBCS-1 sample. This fact is another confirmation of the significant impact of the TARC NPs on the HBCS polymerization network. The spectra at 1638 cm^{-1} corresponding to a substituted amide group overlapped with the corresponding urethane peak[36] formed after the addition of the TARC and APTMS-ZnO. This might be due to the functional groups either the presence of amine groups in the APTMS-ZnO or the substitution reaction between the amine group of the urethane moiety and the carboxylic group in the TARC. It has also been observed that the peaks of the functional groups overlap to form a sharp peak at the amide peak position.

Besides, the newly formed hydrogen bonds between the substituted amine hydrogen and oxygen atoms shown in Scheme 1 can also be attributed to this overlapping, thus contributing to the additional increase of the peak intensity. However, all samples excluding NIPUB and HBCS-3 show the same peak with almost the same intensity. The −N−H stretching vibration of the urethane groups was observed at 1548 cm^{-1} in which the samples HBCS-1 and HBCS-2 exhibit some enhancement in their peak intensity. This observation can be due to the presence of the secondary amine groups in the APTMS-ZnO NPs.

The IR-absorption capacity of the HBCS was studied based on the FTIR spectra ranging from 750 to 1250 cm^{-1} (Figure

https://dx.doi.org/10.1021/acsomega.9b04388
ACS Omega 2020, 5, 10315−10326

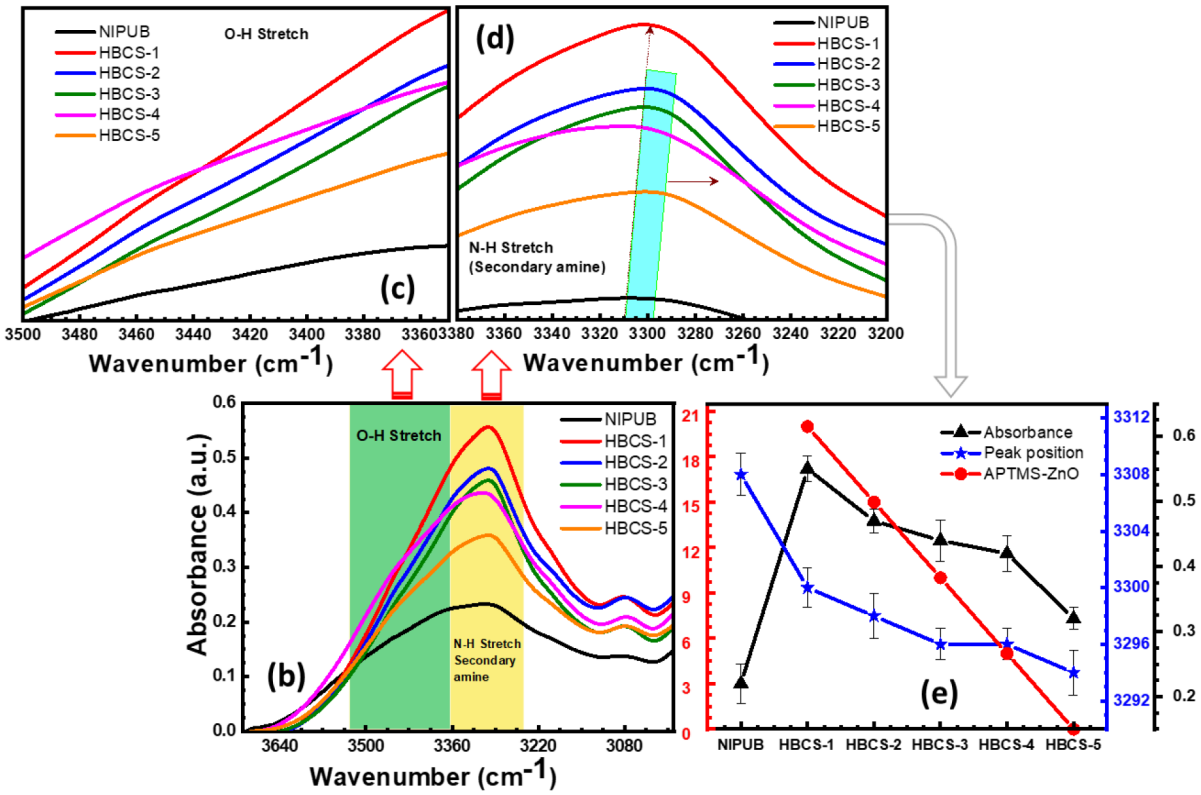

Figure 7. FT-IR spectra of the selected (b) −O−H and −N−H stretching regions; (c) −O−H stretching region; (d) −N−H stretching region of secondary amine; and (e) impact of NPs on the absorption peak height and peak position of the tested samples.

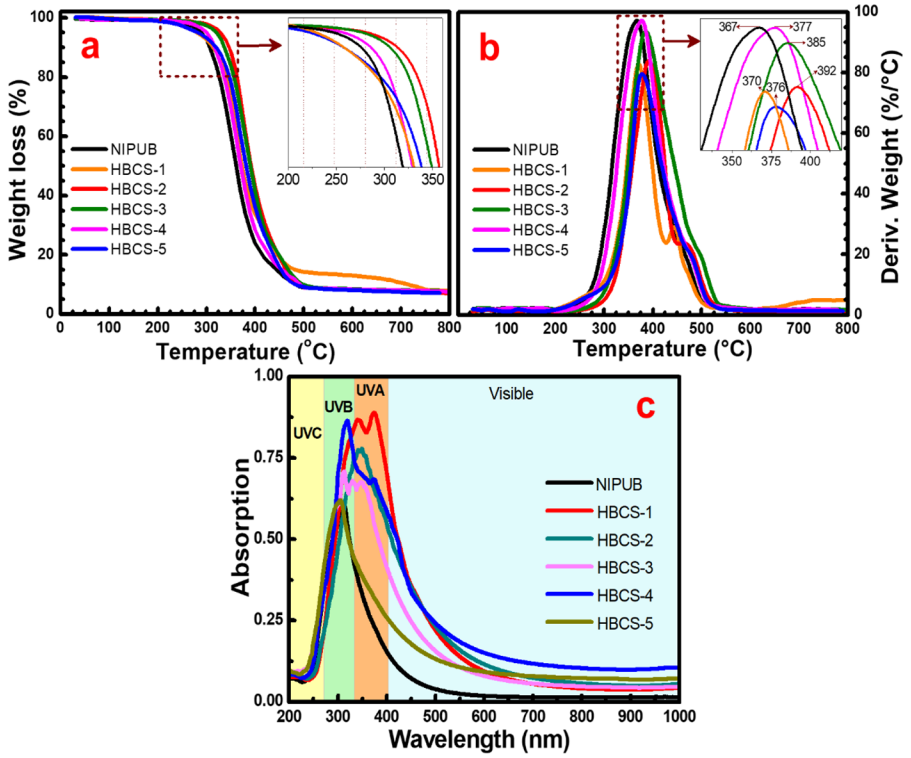

Figure 8. (a) TGA and (b) DTG curves of the HBCS as measured under nitrogen gas; (c) UV−visible spectra of the HBCS incorporated with TARC and APTMS-ZnO NPs. The vertical lines define the spectral ranges UVC, UVB, UVA, and visible regions.

6g). Due to the thermoplastic properties of the NIPHU prepolymer, the pristine NIPUB sample exhibited a weak IR-absorption band within the selected range. The intense peaks of the HBCS sample with 5−25 wt % of NPs at 1176, 1096, 1060, and 772 cm^{-1} showed significant enhancement in their intensity compared to the pristine NIPUB. We attributed this

https://dx.doi.org/10.1021/acsomega.9b04388
ACS Omega 2020, 5, 10315−10326

Table 1. Thermal Properties of the HBCS Incorporated with TARC and APTMS-ZnO NPs

samples	T_{onset} (°C)[a]	T_d (5%) (°C)[a]	T_d (50%) (°C)[a]	char (%)[a]	PH[b]
NIPUB	234	292	367	11	2B
HBCS-1	218	280	370	8	B
HBCS-2	282	334	392	8	H
HBCS-3	263	325	385	8	H
HBCS-4	247	308	377	8	H
HBCS-5	209	283	370	8	B

[a]T_d (5%) and T_d (50%) of the char at 700 °C have been determined from TGA measurements. [b]Pencil hardness.

effect to the overlap of the peaks of the newly formed covalent bond between the −OH group of the TARC and the polymer network (Scheme 1). Besides, the formation of the Si−O barrier layer around the ZnO nanoparticle surface after APTMS treatment also increased the intensity of the IR-absorption peaks. The sample HBCS-2 exhibited maximal IR-absorption capacity compared to other samples.

The effect of APTMS-ZnO and TARC NPs on −O−H and −N−H stretching frequencies was investigated by using the selected FT-IR region from 3500 to 3200 cm^{-1} (Figure 7). The absorption trend of the HBCS evidenced that there was a significant influence on the −O−H and −N−H stretching frequencies. Due to this fact, the selected FT-IR region (Figure 7b) was enlarged and studied deeply (Figure 7c,d) using comparative analysis between the trends of the APTMS-ZnO NP composition, absorbance, and their peak positions (Figure 7e). The broad absorption peak of the pristine NIPUB shows the overlapped −O−H and −N−H stretching frequencies (Figure 7b). Sharp and shifting of absorption peaks with increased intensity toward the longer-wavelength region when the APTMS-ZnO content was increased in the coating system were observed. This observation could be due to two reasons: (i) the formation of hydrogen bonds between the secondary amine present in APTMS-ZnO NPs and the residual hydroxyl groups of the NIPUB polymer network.[37,38] This could be due to the inductive effect of the alkyl group on amine groups attached with it in APTMS-ZnO and the alkyl chain of the polymeric backbone on hydroxyl groups.[37] Thus, the basicity of both the amine nitrogen and hydroxyl oxygen was increased to make their protons involve in the bond formation.[37,38] Therefore, the composite network structure was comprised of OH−N bonds from hydroxyl groups to the amine nitrogen and NH−O bonds from the amine nitrogen to the hydroxyl oxygen,[37] as illustrated in Scheme 1; (ii) the reduction of the hydroxyl groups in both the TARC and the polymeric backbone of the coating matrix, where C_2−OH and C_6−OH groups of the TARC were involved in the bond formation, as illustrated in Scheme 1.

Thermal Stability Study of the HBCS. The thermal stability of the HBCS was evaluated using TGA-DTG analysis, in the temperature ranging from room temperature to 800 °C (Figure 8a,b). Table 1 shows the characteristic temperatures of the HBCS samples for the characterization study of the degradation process. It was obvious that the sample HBCS-2 has the best onset temperature (T_{onset}). This might be due to the stoichiometric distribution and uniform reinforcing density of the TARC and APTMS-ZnO NPs within the HBCS polymer network. Meanwhile, the composites with perfect architectures, i.e., the same stoichiometric ratio (1:1 (w/w)) of NIPHU prepolymer and EJCO such as HBCS-3 and HBCS-4, show a higher T_{onset} and an almost equal amount of char compared to the pristine NIPUB sample. However, the materials having a linear structure, HBCS-1 and HBCS-5, show low T_{onset}. In the HBCS-1 sample, the low T_{onset} can be attributed to the decomposition of the amine content of the APTMS-ZnO NPs, whereas in the case of the HBCS-5 sample, the low T_{onset} was due to the decomposition of the TARC NPs.

In contrast, the degradation temperature of urethane linkages was reported to be lower, ≈ 260 °C, for the NIPHU/epoxy hybrid material system,[39] where polypropylene glycol diglycidyl ether-based CJCO and the epoxy counterpart have been used for the synthesis. It was clear that the HBCS displayed higher degradation temperatures due to the urethane linkages. The trend was almost the same for T_d (50%). However, the materials having a linear structure, HBCS-1 and HBCS-5, have low T_{onset} values.

The thermal stability was seen to be very good for up to about 200 °C. The degradation temperature T_d (5%) of all samples was higher than 280 °C with a maximum of 325 °C for HBCS-3, and this might be the typical degradation temperature of urethane linkages. Table 1 also illustrates the hardness data of the HBCS measured using a pencil hardness tester. Compared to the pristine NIPUB coating, the TARC and APTMS-ZnO NPs exhibited enhanced hardness.

The hardness of the HBCS samples was attributed to the increase of crosslinking density, which usually took place between the hydroxyl moiety of the coating matrix and the functional groups, including the carboxylic and amine groups of the NPs. However, the absence of the APTMS-ZnO nanoparticle content in the coating system will result in a drop in the hardness from H to B (HBCS-5 sample).

UV−visible Absorption Study of the HBCS. The UV absorption ability of the HBCS was investigated with respect to the samples (Figure 8c). The UV absorption of all HBCSs is important in the medium- and long-wave regions, UVB and UVA, respectively. In the short-wave region, the absorption in the UVC ray was lower than 0.25. The pristine NIPUB coating showed a narrow absorption curve with a maximum of about 0.6 at the border between UVB and UVA regions. The addition of APTMS-ZnO in the composite has increased the absorption and broadened and shifted the maximum long-wave region toward the region of UVA. All samples except the HBCS-5 sample showed significant absorption between 0.6 and 0.8 in the UVA region (320 nm < λ < 400 nm). The HBCS-1 sample with 20 wt % of APTMS-ZnO and the HBCS-2 sample with a mixture of respectively 5 and 15 wt % of TARC and APTMS-ZnO showed higher UV absorption values greater than 0.8 and broad absorption curves, which covered almost the whole UVB region (Figure 88c). This might be due to the high content of APTMS-ZnO NPs and their uniform dispersion in the HBCS. HBCS-5 that did not contain any APTMS-ZnO NPs shows low UV absorption as pristine NIPUB. The SEM images of (Figure S1) the pristine NIPUB and HBCS-4 samples showed that the hybrid coating system

https://dx.doi.org/10.1021/acsomega.9b04388
ACS Omega 2020, 5, 10315−10326

Scheme 2. Schematic Illustration of Stepwise Functional Modifications of CJCO from *J. curcas* Oil

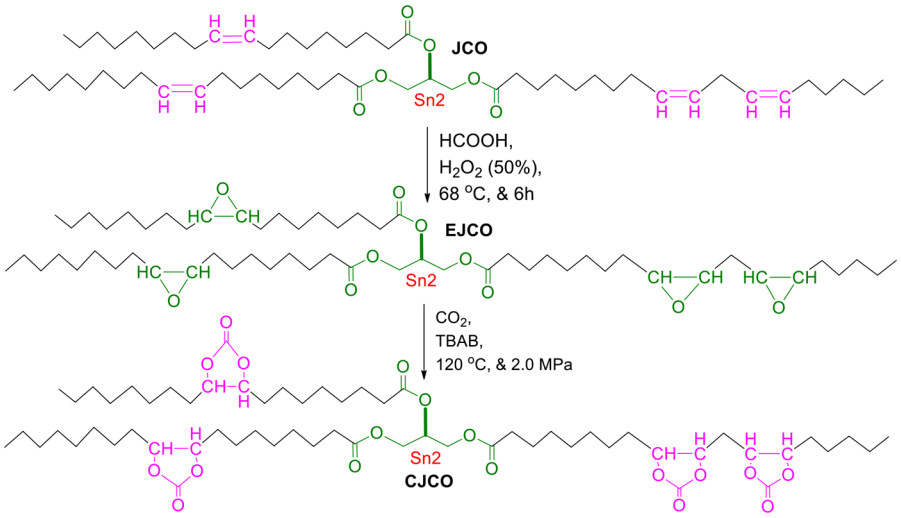

was successfully coated on glass surfaces without any NP aggregation, pinholes, or comet scratches. The morphology of these film surfaces revealed the uniform distribution of the NPs within the polymer matrix. The results indicated that the APTMS-ZnO NPs were responsible for the UV absorption process. At the long-wave edge of the UVA region, the absorption of the HBCS-5 sample was almost twice compared to the absorption of the pristine sample.

CONCLUSIONS

In this study, NIPHU prepolymer/EJCO-based hybrid bionanocomposite coating systems were prepared with the incorporation of TARC and APTMS-ZnO NPs. The hybrid coating system was successfully coated on glass surfaces without any aggregates, pinholes, or comet scratches. Six series of the coating matrix of the −OH-terminated NIPHU prepolymer and EJCO were successfully prepared. The successful ring opening and polymerization of the EJCO and NIPHU prepolymer in the coating matrix were confirmed by ^{1}HNMR and ^{13}C-NMR spectroscopic investigations. The properties of the final HBCS were controlled by varying the compositional mixture of the TARC and APTMS-ZnO NPs. The IR and UV spectra of these coatings show dramatic changes after the incorporation of the TARC and APTMS-ZnO NPs, making these HBCSs attractive for future applications. The study showed that HBCSs with 5% of TARC and 15% of APTMS-ZnO (HBCS-2) exhibited a uniform crosslinking and reinforcement network. However, when the TARC content increased up to 10% (HBCS-3), not only the T_d (50%) of the HBCS dropped to 385 °C from 392 °C, but the IR and UV absorption properties also decreased significantly, which might be a result of the lower content of Si-O-capped ZnO NPs in the HBCS-3 and their weaker reinforcement. It was clear that enhancement in IR absorption can be achieved by the introduction of Si-O-capped ZnO NPs and the inherent reflectivity of wide-gap ZnO NPs. The uniform crosslinking and reinforcement of the network in HBCS-2 provided optimal UV and IR absorption properties to the hybrid bionanocomposite coating system.

EXPERIMENTAL SECTION

Materials. *J. curcas* oil was supplied from Wahum Edible Oil Sdn. Bhd. (Cyberjaya, Malaysia). Microcrystalline cellulose and all the remaining chemicals such as (2,2,6,6-tetramethylpiperidin-1-yl)oxy radical (TEMPO), $Zn(NO_3)_2.4H_2O$, (3-aminopropyl)trimethoxysilane $(H_2N(CH_2)_3Si(OCH_3)_3$, 1,3-diaminopropane (DM), tetrabutylammonium bromide (TBAB), CO_2, tetrahydrofurene (THF), xylene, dimethylformamide (DMF), perchloric acid, denatured ethanol, KOH, sodium bicarbonate, and trimethylamine were purchased from Sigma-Aldrich (Kuala Lumpur, Malaysia).

Synthesis of epoxidized *J. curcas* oil (EJCO) and cyclic carbonate *J. curcas* oil (CJCO). EJCO and CJCO were prepared as described previously elsewhere.[17,40] In brief, *J. curcas* oil (100 g) was epoxidized with hydrogen peroxide (115.6 g, 50% (w/v)) and actuated using 4.6 g of formic acid. A portion of EJCO (100 g), which was already prepared, was used to form CJCO, with the aid of TBAB catalysis (3.5 g) using a pressure reactor at 120 °C and 2.0 MPa,[17] as shown in Scheme 2. TBAB was separated by solvent separation techniques using diethyl ether and vacuum distillation. The viscosity of the samples increased with respect to functional density in the order of JCO>EJCO>CJCO>NIPUB, and the values are listed in Table S1. The reaction mechanisms of epoxidation and cyclic carbonation processes are illustrated at Scheme 3 using equations 1 and 2.

Preparation of the NIPHU Prepolymer and Coating Matrix. The preformed CJCO was used to initiate a cyclic carbonate aminolysis with 1,3-diaminopropane to synthesize the NIPHU prepolymer in the presence of trimethylamine at 70 °C for 4 h in THF as illustrated in equation 3 of Scheme 3.

The coating matrix was produced by blending the NIPHU prepolymer with EJCO (1:1 (w/w)) aided by the action of H_2SO_4 at 70 °C in THF for 1 h. Equations 4 and 5 of Scheme 3 illustrate the reaction mechanisms of the catalyst activity of H_2SO_4 in the epoxy ring-opening reaction and possible nucleophilic attraction of the hydroxyl groups of the prepolymer toward oxirane carbons.

Acid Hydrolyzed, TEMPO-Oxidized, and Rapidly Cooled Cellulose NPs. Carboxylic acid-functionalized cellulose NPs were prepared by a two-step process as described previously.[29] First, 10.2 g of microcrystalline cellulose was

https://dx.doi.org/10.1021/acsomega.9b04388
ACS Omega 2020, 5, 10315−10326

Scheme 3. Schematic Diagram of the Plausible Reaction Mechanism According to the Carbonation and Ring-Opening Polymerization Reactions

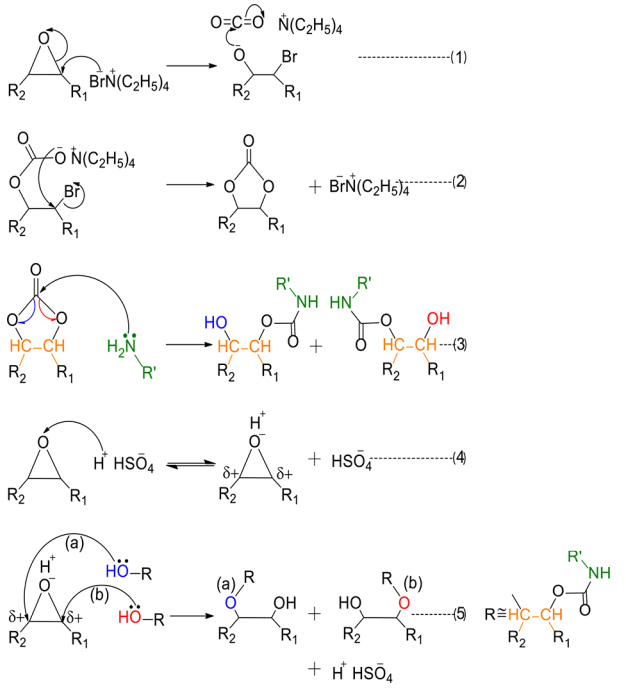

hydrolyzed at 45 °C in a conical flask using 64% sulfuric acid for 130 min. The hydrolysis was quenched by adding ethanol and 10-fold cold Millipore water at a temperature lower than 4 °C. The neutralized freeze-dried cellulose NPs were carboxylic functionalized as illustrated in Scheme 4 using a TEMPO/NaBr/NaClO system with a mole ratio of 0.1 mmol/0.9 mmol/8 mmol/g cellulose in 100 mL Millipore water. The carboxylic functionalization was controlled by the pH of the reaction system. The resultant slurry was freeze-dried to obtain carboxylic acid-functionalized cellulose NPs (TARC).

Scheme 4. Schematic Diagram of Regioselective Oxidation of Cellulose Primary Alcohol Groups

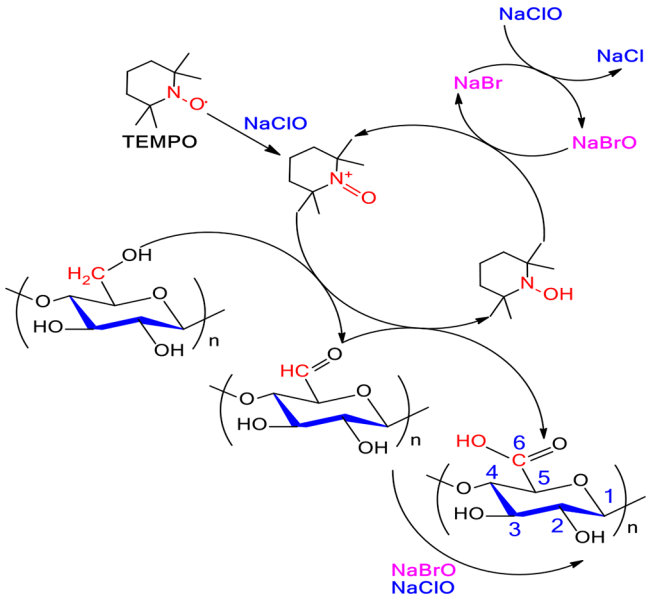

Preparation of APTMS-Treated ZnO NPs (APTMS-ZnO). ZnO NPs were prepared using a technique described elsewhere[41,42] with some modifications, as illustrated in Scheme 5. In detail, zinc nitrate (0.5 M) was added drop by drop to a solution of 0.5 M sodium carbonate under vigorous stirring. The precipitate was then washed thoroughly with distilled water and ethanol, which was then allowed to dry before being placed in an air circulating oven at 80 °C for 2 h. The dry powder was calcined at 650 °C for 3 h and ball-milled to obtain ZnO nanopowder. The prefabricated ZnO NPs (3 g) were dispersed in 100 mL of an ethanol/distilled water mixture (80/20 (v/v)) for 30 min. Then, 2.0 mL of APTMS was applied to the dispersion followed by 130 mL of 95% absolute ethanol and 70 mL of distilled water. The mixture was stirred for 24 h at room temperature. APTMS-ZnO NPs were filtered by gravity filtration, then dried at room temperature for 12 h and ball-milled for 5 h to obtain average size particles of 33.00 nm at 200 rpm.

Fabrication of the Hybrid Bionanocomposite Coating System (HBCS). The coating matrix already formed was used to fabricate the HBCS that comprises TARC and APTMS-ZnO NP suspensions. The suspensions were prepared by dispersing 0.18 g of the respective NPs separately in 100 mL of DMF. Four compositions of HBCS were synthesized with TARC suspensions of 0.3, 0.6, 0.9, and 1.2 g containing 0.4, 0.3, 0.2, and 0.1 g of the APTMS-ZnO suspension, respectively. The xylene and dimethylformamide (80/20 v/v) solvent mixture was used as the coating solvent. The corresponding weight percentages of the nanoparticle suspensions were 5, 10, 15, and 20 wt % for TARC and vice versa for APTMS-ZnO, as presented in Table 2. The HBCSs were cast on glass substrate surfaces using a spin coater and then cured at 90 °C for 72 h.

Characterizations. The molecular weight distribution of the samples was obtained by gel permeation chromatography (GPC-THF system). Fourier transform infrared (FTIR) spectroscopic analysis of the specimens was performed using a PerkinElmer Spectrum 400 FTIR spectrometer (PerkinElmer, Waltham, MA, USA) at room temperature with a resolution of 4 cm^{-1} and 32 scans per recording over a wavenumber range of 4000−400 cm^{-1}. X-ray diffraction (XRD) analysis of the prefabricated ZnO and APTMS-ZnO NPs was performed using a Siemens D5000 system. The crystallite size of the NPs was evaluated from the X-ray powder diffraction data using the Scherrer formula $D_{hkl} = K\lambda/(\beta\cos\theta)$, where D_{hkl} is the mean size of the ordered crystalline grain, K is a dimensionless shape factor (0.89), λ is the X-ray wavelength of the Cu target (0.1542 nm), β is the full width at half maximum (FWHM) intensity (in radians), and θ is the Bragg angle (in degrees). Ultraviolet−visible (UV−vis) absorption spectra were investigated within the wavelength range of 200−1400 nm. The test samples such as *J. curcas* oil, EJCO, CJCO, and NIPUB (10 mg) were dissolved in 0.5 mL of deuterated chloroform ($CDCl_3$) in a 5 mm nuclear magnetic resonance (NMR) tube separately for ^{1}H- and ^{13}C-NMR analyses. Thermal stabilities (TGA and DTG) of the pristine and HBCS samples were determined using a TGA 8516 (Mettler-Toledo DmbH thermoanalyzer), where 10 mg of the samples was heated to 800 °C in a nitrogen atmosphere at room temperature at a heating rate of 10 °C/min. Transmission electron microscopy and SEM were used to examine the morphology of the TARC NPs and film surfaces, respectively.

https://dx.doi.org/10.1021/acsomega.9b04388
ACS Omega 2020, 5, 10315−10326

Scheme 5. Schematic Illustration of the APTMS Treatment of ZnO Nanoparticles

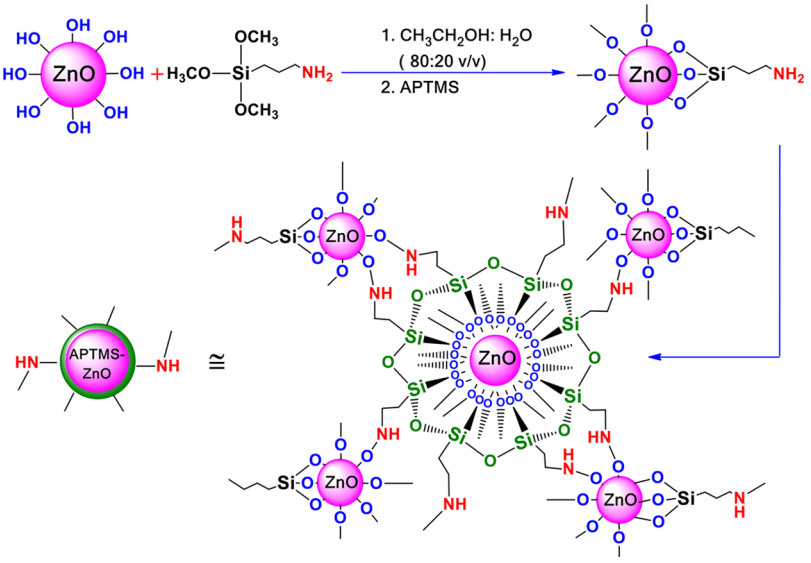

Table 2. Composition (g) of the HBCS Incorporated with TARC and APTMS-ZnO NPs

samples	NIPHU-PP[a]	EJCO	SM[b]	TARC (wt %)	APTMS-ZnO (wt %)
NIPUB	3.0	3.0	1.4		
HBCS-1	3.0	3.0	1.4	0.00	20.00
HBCS-2	3.0	3.0	1.4	5.00	15.00
HBCS-3	3.0	3.0	1.4	10.00	10.00
HBCS-4	3.0	3.0	1.4	15.00	5.00
HBCS-5	3.0	3.0	1.4	20.00	0.00

[a]PP-prepolymer. [b]Solvent mixture.

■ ASSOCIATED CONTENT

Supporting Information

The Supporting Information is available free of charge at https://pubs.acs.org/doi/10.1021/acsomega.9b04388.

Physiochemical properties; comparison of the functional monomers; typical SEM images; comparison of the pristine and nanocomposite samples prepared shown in Figure S1 (PDF).

■ AUTHOR INFORMATION

Corresponding Authors

Hazlee Azil Illias − *Advanced Materials Center, Faculty of Engineering and Department of Electrical Engineering, Faculty of Engineering, University of Malaya, Malaysia, 50603 Kuala Lumpur, Malaysia*; Email: h.illias@um.edu.my

Ching Yern Chee − *Advanced Materials Center, Faculty of Engineering and Department of Chemical Engineering, Faculty of Engineering, University of Malaya, Malaysia, 50603 Kuala Lumpur, Malaysia*; orcid.org/0000-0002-1611-1341; Email: chingyc@um.edu.my

Authors

Mhd. Abd. Cader Mhd. Haniffa − *Advanced Materials Center, Faculty of Engineering, Department of Electrical Engineering, Faculty of Engineering, and Department of Chemistry, Faculty of Science, University of Malaya, Malaysia, 50603 Kuala Lumpur, Malaysia*

Shaliza Ibrahim − *Institute of Ocean and Earth Sciences, Deputy Vice Chancellor (Research & Innovation) Office, University of Malaya, Malaysia, 50603 Kuala Lumpur, Malaysia*

Viorel Sandu − *Dept. Magnetism and Superconductivity, National Institute of Materials Physics, Magurele 077125, Romania*

Cheng Hock Chuah − *Department of Chemistry, Faculty of Science, University of Malaya, Malaysia, 50603 Kuala Lumpur, Malaysia*

Complete contact information is available at: https://pubs.acs.org/10.1021/acsomega.9b04388

Author Contributions

The manuscript was written through contributions from all authors. All authors have given approval to the final version of the manuscript. These authors contributed according to their expertise.

Notes

The authors declare no competing financial interest.

■ ACKNOWLEDGMENTS

The authors would like to acknowledge the financial support from the Ministry of Education of Malaysia PR006-2019A and University of Malaya GPF077A-2018, IIRG 007B-19IISS, and LL046-2019 for the success of this project.

■ REFERENCES

(1) Rabnawaz, M.; Wyman, I.; Auras, R.; Cheng, S. A Roadmap Towards Green Packaging: the Current Status and Future Outlook for Polyesters in the Packaging Industry. *Green Chem.* **2017**, *19*, 4737−4753.

(2) Collins, T. J. Introducing Green Chemistry in Teaching and Research. *J. Chem. Educ.* **1995**, *72*, 965−966.

(3) Miller, S. A. Sustainable Polymers: Opportunities for the Next Decade. *ACS Macro Lett.* **2013**, *2*, 550−554.
(4) Zou, H.; Wu, S.; Shen, J. Polymer/Silica Nanocomposites: Preparation, Characterization, Properties, and Applications. *Chem. Rev.* **2008**, *108*, 3893−3957.
(5) Schottner, G. Hybrid Sol− Gel-Derived Polymers: Applications of Multifunctional Materials. *Chem. Mater.* **2001**, *13*, 3422−3435.
(6) Dalod, A.; Grendal, O.; Blichfeld, A.; Furtula, V.; Pérez, J.; Henriksen, L.; Grande, T.; Einarsrud, M.-A. Structure and Optical Properties of Titania-PDMS Hybrid Nanocomposites Prepared by In Situ Non-Aqueous Synthesis. *Nanomaterials* **2017**, *7*, 460.
(7) Lü, C.; Yang, B. High Refractive Index Organic−Inorganic Nanocomposites: Design, Synthesis and Application. *J. Mater. Chem.* **2009**, *19*, 2884−2901.
(8) Gallon, B. J.; Kojima, R. W.; Kaner, R. B.; Diaconescu, P. L. Palladium Nanoparticles Supported on Polyaniline Nanofibers as a Semi-Heterogeneous Catalyst in Water. *Am. Ethnol.* **2007**, *46*, 7251−7254.
(9) Chee, C. Y.; Yaacob, I. I. Weathering effect on PE coated with thin layer of PU/nanosilica composite. *Adv. Mater. Res.* **2011**, *181−182*, 697.
(10) Leong, W. L.; Lee, P. S.; Lohani, A.; Lam, Y. M.; Chen, T.; Zhang, S.; Dodabalapur, A.; Mhaisalkar, S. G. Non-Volatile Organic Memory Applications Enabled by In Situ Synthesis of Gold Nanoparticles in A Self-Assembled Block Copolymer. *Adv. Mater.* **2008**, *20*, 2325−2331.
(11) Rubentheren, V.; Ward, T. A.; Chee, C. Y.; Nair, P. Physical and chemical reinforcement of chitosan film using nanocrystalline cellulose and tannic acid. *Cellulose* **2015**, *22*, 2529−2541.
(12) Singha, S.; Thomas, M. J.; Insulation, E. Dielectric Properties of Epoxy Nanocomposites. *IEEE Trans. Dielectr. Electr. Insul.* **2008**, *15*, 12−23.
(13) Ching, Y. C.; Chen, Y. C.; Iskandar, I. Y. Mechanical properties changes of nanosilica filled solventborne polyamide binder after accelerated weathering exposure weathering. *Adv. Sci. Lett.* **2012**, *13*, 575−578.
(14) Lu, X.; Zhang, W.; Wang, C.; Wen, T.-C.; Wei, Y. One-Dimensional Conducting Polymer Nanocomposites: Synthesis, Properties and Applications. *Prog. Polym. Sci.* **2011**, *36*, 671−712.
(15) Kiliaris, P.; Papaspyrides, C. D. Polymer/Layered Silicate (Clay) Nanocomposites: An Overview of Flame Retardancy. *Prog. Polym. Sci.* **2010**, *35*, 902−958.
(16) Viorel, S.; Ching, Y. C. Magnetic nanoparticles in MgB2. *Phys. C* **2014**, *498*, 30−37.
(17) Haniffa, M. A. C. M.; Ching, Y. C.; Chuah, C. H.; Kuan, Y. C.; Liu, D.-S.; Liou, N.-S. Synthesis, Characterization and the Solvent Effects on Interfacial Phenomena of *Jatropha Curcas* Oil Based Non-Isocyanate Polyurethane. *Polymers* **2017**, *9*, 162.
(18) Bähr, M.; Bitto, A.; Mülhaupt, R. Cyclic limonene dicarbonate as a new monomer for non-isocyanate oligo- and polyurethanes (NIPU) based upon terpenes. *Green Chem.* **2012**, *14*, 1447−1454.
(19) Blattmann, H.; Fleischer, M.; Bähr, M.; Mülhaupt, R. Isocyanate-and Phosgene-Free Routes to Polyfunctional Cyclic Carbonates and Green Polyurethanes by Fixation of Carbon Dioxide. *Macromol. Rapid Commun.* **2014**, *35*, 1238−1254.
(20) Ochiai, B.; Utsuno, T. Non-Isocyanate Synthesis and Application of Telechelic Polyurethanes Via Polycondensation of Diurethanes Obtained from Ethylene Carbonate and Diamines. *J. Polym. Sci. A1.* **2013**, *51*, 525−533.
(21) Poussard, L.; Mariage, J.; Grignard, B.; Detrembleur, C.; Jérôme, C.; Calberg, C.; Heinrichs, B.; De Winter, J.; Gerbaux, P.; Raquez, J.-M.; Bonnaud, L.; Dubois, P. Non-Isocyanate Polyurethanes from Carbonated Soybean Oil using Monomeric or Oligomeric Diamines to Achieve Thermosets or Thermoplastics. *Macromolecules* **2016**, *49*, 2162−2171.
(22) Tan, Y.; Liu, Y.; Chen, W.; Liu, Y.; Wang, Q.; Li, J.; Yu, H. Homogeneous Dispersion of Cellulose Nanofibers in Waterborne Acrylic Coatings with Improved Properties and Unreduced Transparency. *ACS Sustainable Chem. Eng.* **2016**, *4*, 3766−3772.
(23) Habibi, Y. Key Advances in the Chemical Modification of Nanocelluloses. *Chem. Soc. Rev.* **2014**, *43*, 1519−1542.
(24) Morandi, G.; Heath, L.; Thielemans, W. Cellulose Nanocrystals Grafted with Polystyrene Chains Through Surface-Initiated Atom Transfer Radical Polymerization (Si-ATRP). *Langmuir* **2009**, *25*, 8280−8286.
(25) Bai, Y.; Koh, C. G.; Boreman, M.; Juang, Y.-J.; Tang, I.-C.; Lee, L. J.; Yang, S.-T. Surface Modification for Enhancing Antibody Binding on Polymer-Based Microfluidic Device for Enzyme-Linked Immunosorbent Assay. *Langmuir* **2006**, *22*, 9458−9467.
(26) Hasani, M.; Cranston, E. D.; Westman, G.; Gray, D. G. Cationic Surface Functionalization of Cellulose Nanocrystals. *Soft Matter* **2008**, *4*, 2238−2244.
(27) Amanov, A.; Cho, I.; Pyoun, Y.; Lee, C.; Park, I. Micro-Dimpled Surface by Ultrasonic Nanocrystal Surface Modification and Its Tribological Effects. *Wear* **2012**, *286*, 136−144.
(28) Eyley, S.; Thielemans, W. Surface Modification of Cellulose Nanocrystals. *Nanoscale* **2014**, *6*, 7764−7779.
(29) Haniffa, M. A. C. M.; Ching, Y. C.; Chuah, C. H.; Ching, K. Y.; Nazri, N.; Abdullah, L. C.; Nai-Shang, L. Effect of TEMPO-Oxidization and Rapid Cooling on Thermo-Structural Properties of Nanocellulose. *Carbohydr. Polym.* **2017**, *173*, 91−99.
(30) Haniffa, M. A. C. M.; Ching, Y.; Abdullah, L.; Poh, S.; Chuah, C. Review Of Bionanocomposite Coating Films and Their Applications. *Polymers* **2016**, *8*, 246.
(31) Åkerholm, M.; Hinterstoisser, B.; Salmén, L. Characterization of the Crystalline Structure of Cellulose Using Static and Dynamic FT-IR Spectroscopy. *Carbohydr. Res.* **2004**, *339*, 569−578.
(32) Ching, Y. C.; Iskander, I. Y. Effect of polyurethane/nanosilica composites coating on thermo-mechanical properties of polyethylene film. *Mater. Technol.* **2012**, *27*, 113−115.
(33) Lee, J.; Choi, S.; Bae, S. J.; Yoon, S. M.; Choi, J. S.; Yoon, M. Visible Light-Sensitive Aptes-Bound ZnO Nanowire Toward A Potent Nanoinjector Sensing Biomolecules in A Living Cell. *Nanoscale* **2013**, *5*, 10275−10282.
(34) Jaramillo, A. F.; Baez-Cruz, R.; Montoya, L. F.; Medinam, C.; Pérez-Tijerina, E.; Salazar, F.; Rojas, D.; Melendrez, M. F. Estimation of the Surface Interaction Mechanism of ZnO Nanoparticles Modified with Organosilane Groups by Raman Spectroscopy. *Ceram. Int.* **2017**, *43*, 11838−11847.
(35) Shi, H.-Q.; Li, W.-N.; Sun, L.-W.; Liu, Y.; Xiao, H.-M.; Fu, S.-Y. Synthesis of Silane Surface Modified ZnO Quantum Dots with Ultrastable, Strong and Tunable Luminescence. *Chem. Commun.* **2011**, *47*, 11921−11923.
(36) Srivastava, R. M.; Neves Filho, R. A. W.; da Silva, C. A.; Bortoluzzi, A. J. First ultrasound-mediated one-pot synthesis of N-substituted amides. *Ultrason. Sonochem.* **2009**, *16*, 737−742.
(37) Ching, Y. C.; Kalyani, N.; Khalid, M.; Yoong, W. Optical and structural characterization of solution processed zinc oxide nanorods via hydrothermal method. *Ceram. Int.* **2014**, *40*, 9997−10004.
(38) Kolev, S. K.; Petkov, P. S.; Rangelov, M. A.; Vayssilov, G. N. Density functional study of hydrogen bond formation between methanol and organic molecules containing Cl, F, NH_2, OH, and COOH functional groups. *J. Phys. Chem. A* **2011**, *115*, 14054−14068.
(39) Ke, J.; Li, X.; Wang, F.; Jiang, S.; Kang, M.; Wang, J.; Li, Q.; Wang, Z. Non-isocyanate polyurethane/epoxy hybrid materials with different and controlled architectures prepared from a CO_2-sourced monomer and epoxy via an environmentally-friendly route. *RSC Adv.* **2017**, *7*, 28841−28852.
(40) Gogoi, P.; Boruah, M.; Sharma, S.; Dolui, S. K. Blends of epoxidized alkyd resins based on jatropha oil and the epoxidized oil cured with aqueous citric acid solution: a green technology approach. *ACS Sustainable Chem. Eng.* **2015**, *3*, 261−268.
(41) Haniffa, M. A. C. M.; Ching, Y. C.; Chuah, C. H.; Kuan, Y. C. Nai-Shang Liou, Synergistic effect of (3-Aminopropyl)-Trimethoxysilane treated ZnO and corundum nanoparticles under UV-irradiation on UV-cutoff and IR-absorption spectra of acrylic polyurethane based nanocomposite coating. *Polym. Degrad. Stab.* **2018**, *159*, 205−216.

https://dx.doi.org/10.1021/acsomega.9b04388
ACS Omega 2020, 5, 10315−10326

(42) Han, Z.; Wang, X.; Heng, C.; Han, Q.; Cai, S.; Li, J.; Qi, C.; Liang, W.; Yang, R.; Wang, C. Synergistically enhanced photocatalytic and chemotherapeutic effects of aptamer-functionalized ZnO nanoparticles towards cancer cells. *Phys. Chem. Chem. Phys.* **2015**, *17*, 21576−21582.

https://dx.doi.org/10.1021/acsomega.9b04388
ACS Omega 2020, 5, 10315−10326